RSC Advances

PAPER

View Article Online
View Journal | View Issue

Cite this: *RSC Adv.*, 2024, **14**, 15155

Portable hydroxyl-functionalized coal gangue-based cordierite porous ceramics sheets for effective adsorption of fluorine-containing wastewater

Deyin Wang,[ab] Liming Guo,[ab] Zhennan Qiao,[ab] Hongwei Liu,[ab] Yanlan Zhang[ab] and Yongzhen Wang *[ab]

Monolithic adsorbent removal of fluoride from water is considered an effective and non-secondary pollution method. Here, a portable hydroxyl-functionalized coal gangue-based cordierite porous ceramic sheet (ACGC-Fe) is prepared by using coal gangue solid waste with a specific silicon-aluminum-rich composition ratio and a small amount of magnesium oxide as a raw material through powder compression molding and mild chemical modification. The prepared ACGC-Fe can be used to treat fluorine-containing wastewater and the maximum adsorption of fluorine can reach 18.69 mg g^{-1}. The Langmuir (Freundlich) adsorption isotherm model and pseudo-second-order kinetic model here provided a satisfactory description of the fluoride removal operating mechanism, and it is confirmed that the adsorption mechanism of ACGC-Fe is mainly attributed to the chemisorption of hydrogen bonds (with hydroxyl group) and ionic bonds (with metal), and physical adsorption based on cordierite porous ceramic pores. This research will provide a new idea for designing high-performance materials by mining and analyzing the composition and structure characteristics of coal gangue solid waste itself and broaden the application range of high-value-added coal gangue solid waste.

Received 13th March 2024
Accepted 1st May 2024

DOI: 10.1039/d4ra01928h

rsc.li/rsc-advances

Introduction

Fluorine is a vital trace element for the human body. However, due to the ongoing progress of different industries,[1,2] it has emerged as a significant contributor[3] to water pollution. Fluoride exhibits a high attraction to calcium and phosphorus[4] in the human body, potentially leading to the development of various diseases.[5] Various methods have been employed for treating fluorine-containing wastewater, including adsorption,[6] coagulation precipitation, ion exchange,[7] membrane filtration, and electrochemical methods.[4] Among these methods, adsorption methods are preferred due to their simplicity, efficiency,[8] economic feasibility, and sustainability. Jadhav and Jadhav[9] utilized black mustard shell fly ash (BMHFA) to achieve a high fluoride absorption capacity of 4.42 mg g^{-1}. Although these adsorbent materials demonstrate strong adsorption capabilities, they are hindered by challenges such as limited recyclability. The porous magnesium oxide nanosheets successfully synthesized by Jin *et al.*[10] using a precursor calcination method can be used as potential suitable candidates for fluoride removal. Monolithic materials can obviously effectively address the issue of recyclability, however, their high preparation cost and the potential for dissolution during the adsorption process leading to secondary pollution[11] are these adsorbent materials major drawbacks. Therefore, the development of adsorbents that are shaped, recyclable, and do not cause secondary pollution holds greater practical application value.

Ceramic materials exhibit high corrosion resistance and can be easily molded into various shapes such as blocks or tablets. This property makes them ideal for addressing issues related to recyclability and secondary pollution in wastewater adsorption processes. However, the high cost of ceramic materials often hinders their widespread application. Therefore, seeking low-cost and widely sourced raw materials can effectively reduce the cost of ceramic adsorbent materials to realize their practical application value.

Coal gangue stands as one of the largest solid wastes of the industrial sector in the world,[12] and its accumulation not only occupies significant land space,[13] but also causes pollution to the atmosphere,[14] water and soil,[15] posing a significant threat to both humans and the ecological system.[16] However, the current utilization of coal gangue remains primarily restricted to low-value applications such as power generation,[17,18] building materials,[19] filling materials for coal mine graves,[19] and land reclamation. Although the bulk consumption of coal gangue has been

[a]College of Materials Science and Engineering, Taiyuan University of Technology, Taiyuan 030024, China. E-mail: wangyongzhen@tyut.edu.cn
[b]Shanxi Joint Laboratory of Coal based Solid Waste Resource Utilization and Green Ecological Development, Taiyuan 030024, China

achieved, which can effectively solve the storage problem of coal gangue solid waste, its utilization value is low, and it is still necessary to further explore the characteristics of coal gangue to further realize its high value-added utilization. Currently, coal gangue solid waste is being utilized in the production of molecular sieves,[20] ceramics,[21] and aluminum-based chemical raw materials.[22] Due to its high content of Al_2O_3 and SiO_2, coal gangue is commonly utilized as a raw material in the production of synthetic ceramics. Cordierite porous ceramics are known for their high-temperature resistance, acid, and alkali resistance, and impressive compressive strength. Research by Zhang *et al.*[23] demonstrated that modified mullite whiskers/cordierite ceramic samples have a strong adsorption effect for Cu^{2+}. Additionally, Yang *et al.*[24] found that oxalic acid-modified cordierite honeycomb ceramics are highly efficient in removing azo neutral red dyes (NR) from water. Despite these findings, there are still few studies on fluorine adsorption by cordierite porous ceramics.

To address these issues, this study designed and prepared portable hydroxyl-functionalized coal gangue-based cordierite porous ceramics sheets for treating fluorine-containing wastewater based on the composition characteristics of coal gangue solid waste (material-based directional design). The adsorbent comprises two components: a cordierite porous ceramics matrix and a surface modification. The raw material for the matrix is coal gangue, with proportions of its components SiO_2 and Al_2O_3 matching those required in cordierite. Cordierite can be directly synthesized by simply adding MgO. Enhancing the specific surface area through acid treatment can effectively improve the removal of fluoride in such ceramics.[25] The surface modifier used is polyhydroxy iron, known for its exceptional fluorine removal capabilities. Therefore, combining the two components to form an integral adsorbent can achieve a more effective fluoride removal effect.

Materials and methods

Materials

In this research, the coal gangue (CG) sample utilized was acquired from Xing County, Lvliang City, Shanxi Province, China. The chemical reagents MgO (98%), ethanol, HCl (37%), NaOH, NaF (98%), Na_2CO_3, and $Fe(NO_3)_3 \cdot 9H_2O$ (98.5%) were procured from Sinopharm Chemical Reagent Co. Furthermore, the experiment employed self-made ultrapure water as the experimental medium.

Methods

Preparation of coal gangue-based cordierite porous ceramics sheet (CGC). The initial crushing of the coal gangue involved the utilization of a jaw crusher, followed by sieving it through a 200 mesh sieve. As a subsequent step, the coal gangue was employed as a source of silicon and aluminum. The mass ratio of CG to MgO was determined as 555 : 81 based on the theoretical ratio of cordierite Mg : Al : Si = 2 : 4 : 5. The appropriate amount of raw materials (555 mg coal gangue and 81 mg MgO) was accurately weighed, and mixed in an agate mortar, with 1 mL ethanol added for grinding for 2 minutes until a homogeneous mixture was obtained. The resulting mixture was then pressed and molded on a tablet press, resulting in the formation of the CGC precursor. The CGC was achieved by placing the precursor in a corundum crucible and applying gradient heating in a tube furnace. To begin with, the temperature was gradually raised to 600 °C at a rate of 3 °C min^{-1} and maintained for 0.5 hours. Following that, in the second phase, the temperature was further elevated to 1250 °C at a rate of 2 °C min^{-1} and held for 1.5 hours. Ultimately, the samples were cooled to ambient temperature using the furnace, resulting in the formation of the CGC.

Preparation of active coal gangue-based cordierite porous ceramics sheet (ACGC). To prepare the ACGC, a specific amount of CGC was added to a hydrochloric acid solution with a concentration of 2.5 mol L^{-1} at a solid–liquid ratio of 1 : 10. The mixture was then subjected to hydrothermal reaction at a temperature of 90 °C for 2 hours. Subsequently, the residual hydrochloric acid in the CGC was removed by washing multiple times with ultrapure water until the pH of the washing solution became 7, and the washing was completed. Finally, the washed CGC was dried in a vacuum drying oven at 50 °C until the weight was constant to obtain ACGC.

Preparation of hydroxyl-functionalized coal gangue-based cordierite porous ceramics sheet (ACGC-Fe). We first vacuum-impregnated ACGC and polyhydroxy iron solution (see the ESI[26] for the preparation method) at a temperature of 60 °C for 2 hours. This process was carried out by maintaining a solid–liquid ratio of 1 : 2. Subsequently, we eliminated any surplus solution present on the surface of ACGC by gently blotting it with filter paper. ACGC-Fe was obtained in an oven set at 60 °C.

Characterization

To systematically characterize the coal gangue and the synthesized samples, a range of characterization methods were employed. X-ray fluorescence spectrometry (XRF) was employed to determine the composition and content of coal gangue. The weight loss of coal gangue at different temperatures was measured using a thermogravimetric analyzer (TG, NETZSCH STA 449F5). X-ray diffraction (XRD, Bruker D8-advance) with Cu Kα radiation at 40 kV was used to identify the physical phases. The surface morphology and microstructure were observed using a scanning electron microscope (SEM, ZEISS Gemini 300) at 5.0 kV. The specific surface area and pore size distribution were determined by employing a micropore physical adsorption meter (Micromeritics ASAP 2020 PLUS HD88) at 77 K. Fourier transform infrared spectroscopy (FTIR, Nicolet iS20) was used to analyze the functional groups and chemical bonds present in the samples within the wave number range of 4000–400 cm^{-1}. X-ray photoelectron spectroscopy (XPS, ESCALAB 250Xi) was utilized to determine the elemental composition and chemical state of the samples. The XPS spectra were fitted using the Gauss–Lorentz curve fitting method (O 1s).

Adsorption experiments

Experiments were conducted using centrifuge tubes or conical flasks to study the impact of different factors on the adsorption of fluoride by ACGC-Fe. These factors included solution pH (3–

10), initial concentration of the solution (100–800 mg L^{-1}), ambient temperature (298.15–318.15 K), adsorption time (0–1440 min), and amount of adsorbent (50–450 mg). The adsorption experiments were carried out utilizing a dual-function gas-bath thermostatic shaker (ZD-85) performing at a velocity of 180 revolutions per minute (rpm). An ionic strength agent (0.1 mol L^{-1} NaCl) was added in equal volume to all samples. The concentration of residual fluoride ions was measured by employing an ion meter PXSJ-216F. The tests were conducted repeatedly in batches, with each batch repeated at least three times and the average of the results was computed. The adsorption amount q_e (mg g^{-1}) and adsorption efficiency R (%) of fluoride ions were calculated using eqn (1)[27] and (2)[28] respectively:

$$q_e = \frac{(C_0 - C_e) \times V}{m} \quad (1)$$

$$R = \frac{C_0 - C_e}{C_0} \times 100\% \quad (2)$$

where C_0 (mg L^{-1}) represents the initial concentration of the solution, C_e (mg L^{-1}) refers to the concentration of the solution in the equilibrium stage of adsorption, V (L) represents the volume of the solution, and m (mg) represents the mass of the adsorbent.

Results and discussion

Characterization of coal gangue

Table 1 presents the chemical composition analysis of coal gangue. The research revealed that the predominant constituents within coal gangue are SiO_2, Al_2O_3, and MgO, constituting approximately 87% of its overall makeup. The ratio of SiO_2 to Al_2O_3 in coal gangue is equivalent to the Si : Al needed for cordierite formation. Cordierite can be synthesized directly by incorporating MgO. Additionally, there are trace amounts of other oxides present, such as Fe_2O_3, CaO, TiO_2, K_2O, Na_2O, and others. Fig. 1(a) illustrates the TG curve of the coal gangue. As the temperature increases from 50 °C to 1200 °C at a rate of 10 °C min^{-1}, the TG curve can be categorized into three distinct stages. Initially, the first stage exhibits a mass decrease followed by a slight mass increase. The slight mass increase is attributed to the chemical adsorption behavior of oxygen;[29] the second stage exhibits a significant reduction in mass, corresponding to the release and combustion of volatile and carbonaceous substances contained in the coal gangue;[30] and the third stage demonstrates a slight decrease in mass, likely due to mineral decomposition.[31] Fig. 1(b) presents the XRD pattern of coal gangue, demonstrating the predominance of kaolinite and quartz (SiO_2) in its composition.

Effect of preparation conditions on CGC synthesis

Effect of sintering temperature on CGC synthesis. According to Fig. 2(a), when the temperature is 1200 °C for 120 min, cordierite becomes the main phase in the samples. The characteristic peak shape of cordierite is observed. The diffraction peaks at 2theta = 10.46°, 18.06°, 18.99°, 21.73°, 26.32°, 28.47°, and 29.43° correspond to the cordierite (PDF#99-0035) crystalline surface (110), (310), (002), (112), (312), (222), and (421). When the time is held constant, the intensity of these characteristic diffraction peaks initially increases and then decreases as the temperature increases. The cordierite phase disappears at a temperature of 1400 °C.

Table 1 Composition analysis of coal gangue

Composition	SiO_2	Al_2O_3	Fe_2O_3	CaO	TiO_2	K_2O	MgO	Na_2O	Else
Content/%	51.728	35.666	4.451	2.592	2.112	1.249	0.345	0.136	1.721

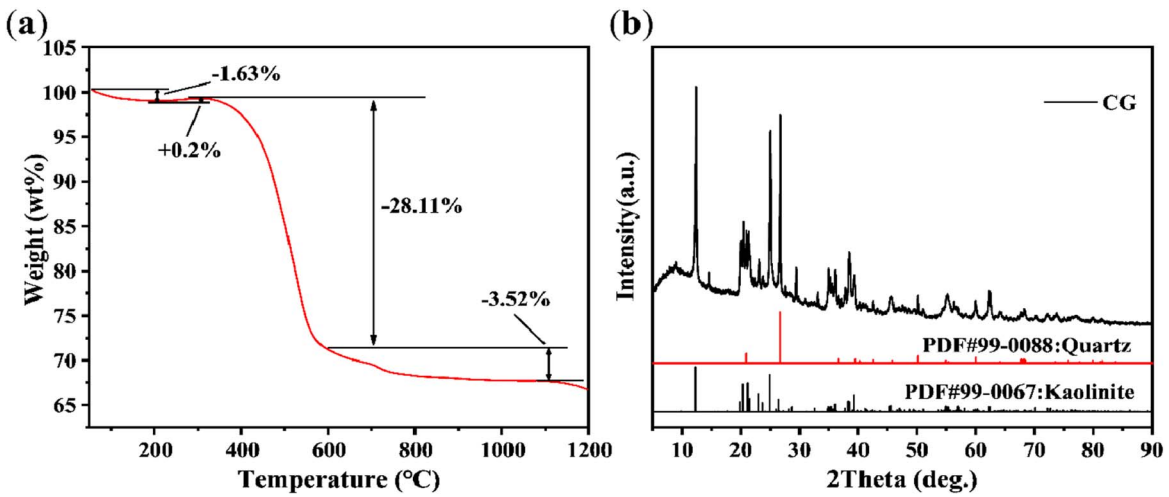

Fig. 1 (a) TG and (b) XRD pattern of coal gangue (CG).

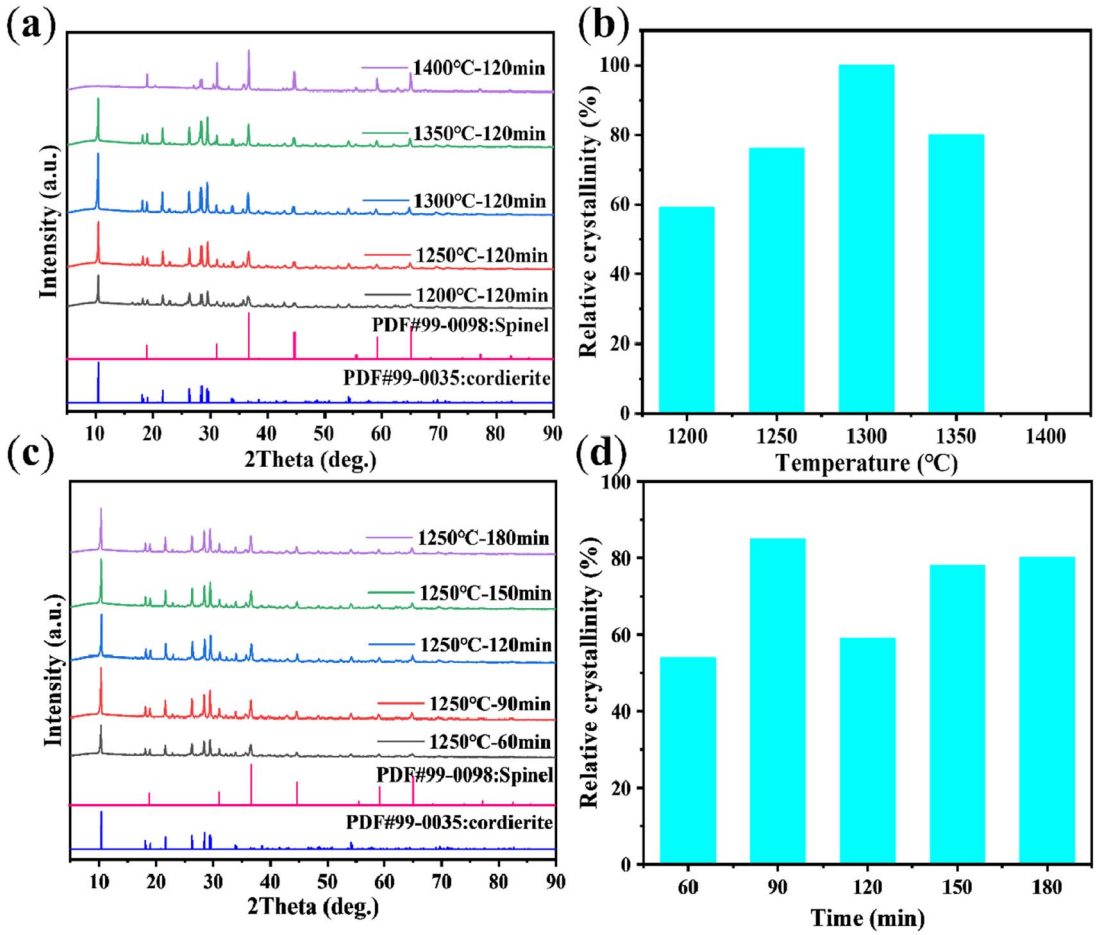

Fig. 2 Effect of CGC synthesized at different crystallization temperatures (crystallization time = 120 min) (Note: (b) 1400 °C did not generate cordierite phase, so the relative crystallinity of zero). (a) XRD patterns, (b) relative crystallinity. Effect of CGC synthesized during various durations of crystallization (crystallization temperature = 1250 °C). (c) XRD patterns, (d) relative crystallinity.

The relative crystallinity was determined by calculating the percentage of the diffraction peak area between (2theta) = 5–30.05° in the sample as compared to the diffraction peak area of the reference sample at the same range.[32] For the calculation of the relative crystallinity (RC), the reference sample chosen was the one possessing optimal crystallinity (sintering temperature of 1300 °C and holding time of 120 min). The RC (%) was converted by the following eqn (3):

$$\mathrm{RC} = (\text{the diffraction peak area of the sample at (2theta) = 5–30.05°})/(\text{the diffraction peak area of the reference sample at the same range}) \quad (3)$$

As shown in Fig. 2(b), the relative crystallinity of the samples reaches a maximum of 76% at the sintering temperature of 1250 °C. However, further increasing the sintering temperature does not significantly enhance the relative crystallinity. And the relative crystallinity drops to 0 at 1400 °C. Therefore, for economic and energy consumption considerations, the optimal sintering temperature is determined to be 1250 °C.

Effect of holding time on CGC synthesis. XRD analysis was conducted on the CGC samples synthesized at a sintering temperature of 1250 °C with varying holding times. The XRD pattern of Fig. 2(c) illustrates that cordierite was the predominant phase in the samples at all holding times. The trend observed in the intensity of cordierite's characteristic diffraction peaks displayed an initial increase followed by a subsequent becomes basically stable within the fluctuation range as the holding times lengthened. We can explain this situation by saying that in the initial stage, cordierite has just begun to crystallize and the relative crystallinity is very low. As the holding time increases, the cordierite grain size gradually increases and the relative crystallinity begins to increase. Finally, cordierite is completely formed. The grain size changes within a reasonable range so that the relative crystallinity also fluctuates within a certain range. The corresponding relative crystallinity values for each holding time of Fig. 2(d) were determined as follows: 54%, 85%, 59%, 78%, and 80%. Therefore, taking into account energy consumption and relative crystallinity, the highest relative crystallinity and shortest holding time (90 min) was deemed as the ideal time for the synthesized samples.

XRD analysis of CGC, ACGC, and ACGC-Fe

Fig. 3(a) showcases the XRD patterns of CGC, ACGC, and ACGC-Fe. The characteristic peaks of ACGC and ACGC-Fe became

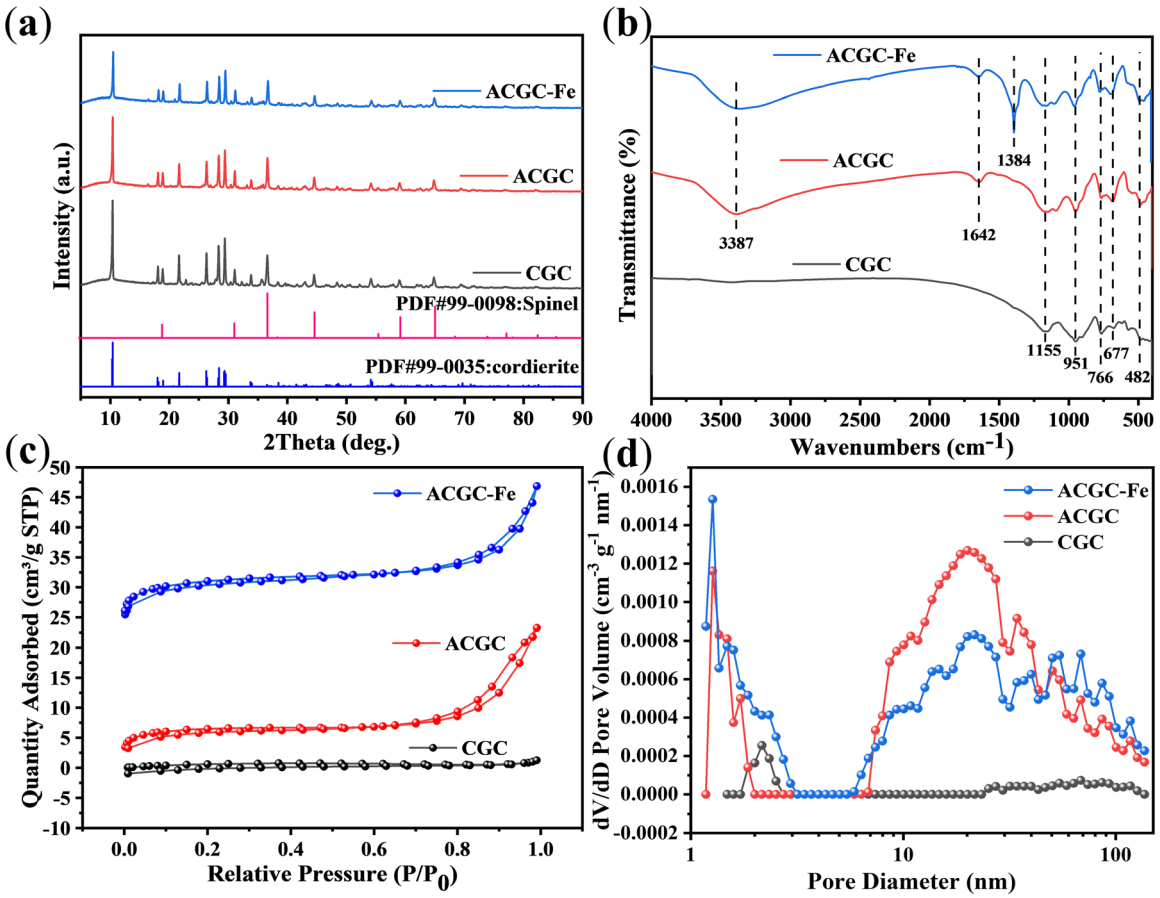

Fig. 3 (a) XRD patterns, (b) FTIR spectra, (c) N_2 adsorption–desorption isotherms at 77 K, (d) pore-size distribution of CGC, ACGC, and ACGC-Fe.

weaker compared to CGC. However, the positions of the diffraction peaks of CGC, ACGC, and ACGC-Fe remain unchanged. This indicates the persistency of the crystalline structure following both acid treatment and surface modification.

FTIR analysis of CGC, ACGC, and ACGC-Fe

Fig. 3(b) depicts the FTIR spectra of CGC, ACGC, and ACGC-Fe. Within the ACGC spectrum, the stretching vibration of –OH[33] is symbolized by the peak at 3387 cm^{-1}, while the bending vibrations caused by adsorbed water[34] are indicated by the peak at 1642 cm^{-1}. The –OH results from the dissolution of Mg^{2+} and Al^{3+} by CGC during acid leaching, as confirmed by XPS. ACGC-Fe, on the other hand, is formed through the surface modification of ACGC with polyhydroxy iron, and the polyhydroxy iron itself has –OH present. As a result, it will overlap with the peaks in ACGC, leading to no significant difference. And it is calculated that the mass of polyhydroxy iron used for surface modification accounts for about 10% of the mass of ACGC-Fe. Therefore, various evidences indicate that the modification was successful. Additionally, ACGC-Fe exhibits a peak at 1384 cm^{-1},[35] which can be attributed to the presence of residual reactant CO_3^{2-} in the polyhydroxy iron solution being adsorbed on ACGC-Fe. The remaining infrared peaks present in all samples consist of the absorption peak of Si–O, the symmetric stretching vibrational absorption peak of the Si–OH end group, the symmetric stretching vibrational absorption peak of the SiO_4 tetrahedron, the bending vibrational peak of Si–O–H,[24] and the Fe–O stretching vibrational peaks.[36] These peaks correspond to 1155 cm^{-1}, 951 cm^{-1}, 766 cm^{-1}, 677 cm^{-1}, and 482 cm^{-1}, respectively.

BET analysis of CGC, ACGC, and ACGC-Fe

In order to determine the specific characteristics of surface area and pore size in the three samples, a series of N_2 adsorption–desorption tests were carried out at 77 K. The isotherms of N_2 adsorption–desorption and the distributions of pore size for all samples can be seen in Fig. 3(c) and (d) respectively. It has been observed that the N_2 adsorption–desorption isotherms of all samples display features typical of type I–IV isotherms,[37] indicating the existence of both microporous and mesoporous structures. The presence of H4-type hysteresis loops further confirms this finding. Additionally, the plots depicting the distribution of pore sizes illustrate the existence of macropores alongside micropores and mesopores. The values in terms of specific surface area for the three samples are as follows: ACGC-Fe (31.80 $m^2\ g^{-1}$) > ACGC (22.94 $m^2\ g^{-1}$) > CGC (2.65 $m^2\ g^{-1}$). The introduction of acid impregnation to CGC resulted in the creation of varying quantities of micropores, mesopores, and macropores, ultimately leading to a noteworthy increase in the specific surface area of ACGC. Moreover, the incorporation of

polyhydroxy iron onto the surface of ACGC also contributed to the enhancement of its specific surface area.

SEM analysis of CGC, ACGC, and ACGC-Fe

SEM was employed to observe the morphological characteristics of CGC, ACGC, and ACGC-Fe, as illustrated in Fig. 4. The morphology of CGC closely resembled that of commercial cordierite porous ceramics,[23] displaying a rough surface and high porosity, suggesting a good adsorption potential. ACGC exhibited an increase in large pores on some areas of its surface, while other areas transitioned from a regular and smooth shape to a rough and uneven texture, characterized by numerous pits and small particles, resulting in the formation of micropores and mesopores.[24] The findings obtained from the BET test also align with this observation. We believe that the reasons for the uneven structure of ACGC in Fig. 4(b) are: the CGC itself has different pore wall thicknesses as shown in Fig. 4(a). After hydrothermal corrosion by HCl, the thin pore walls will inevitably become *via*. The pores with thick pore walls will only undergo surface erosion. Furthermore, CGC contained the phase generated by our reaction (stable chemical structure) and the remaining oxides in the unreacted raw material coal gangue. After undergoing HCl hydrothermal reaction, the oxides will be removed, resulting in large holes in some parts and only surface erosion in other parts. Fig. 4(c) illustrates one side of ACGC-Fe, where no holes are visible, indicating the successful surface modification of polyhydroxy iron.

XPS analysis of CGC, ACGC, and ACGC-Fe

X-ray photoelectron spectroscopy (XPS) allows for the analysis of the composition and the presence of elements present on the surface of samples. Fig. 5(a) displays the XPS spectra for CGC, ACGC, and ACGC-Fe samples. All samples contain the following elements: magnesium (Mg), aluminum (Al), silicon (Si), oxygen (O), and carbon (C). The presence of iron (Fe) in ACGC-Fe, as opposed to CGC and ACGC, implies the effective incorporation of polyhydroxy iron onto the surface of ACGC. This validates the achievement of successful modification. Fig. 5(b), (c), and (d) depict the positions and intensities of the peaks corresponding to Si 2p, Al 2p, and Mg 1s in CGC and ACGC, respectively. It can be observed that the Si 2p content increases from 12.6% in CGC to 14.16% in ACGC, while the Al 2p and Mg 1s contents decrease from 11.46% and 4.56% in CGC to 8.67% and 2.95% in ACGC, respectively, further supporting the findings in FTIR.

Adsorption properties

Effect of pH. Fig. 6(a) presents the influence of pH on the adsorption and removal rate of fluorine. It is evident that the initial pH played a crucial role in the levels of fluorine adsorption and removal. With an increase in pH, the adsorption capacity and elimination of fluorine first increase and then decrease. The optimum pH was found to be 4, which corresponded to an adsorption amount of 15.19 mg g^{-1} and a removal rate of 61.9%. The pK_a of HF was determined to be 3.16. When the pH was less than 3.2,[38] fluorine would be protonated to form HF or HF^{2-} (as shown in eqn (4) and (5)),[39] resulting in the adsorption of very little free fluorine and consequently low adsorption amount and removal rate. When the pH is greater than 4, due to the residual CO_3^{2-}, which is also an anion, on ACGC-Fe, it occupies a certain adsorption site. As the pH value increases, the H^+ concentration becomes lower, and the adsorption sites that can be reacted and released gradually decrease. Therefore, the adsorption capacity and removal rate gradually decrease. On the other hand, when the pH was greater than 7, the concentration of OH^- in the solution increased, leading to competition with fluorine for adsorption sites. This reduced the likelihood of adsorption between fluorine and the adsorbent, resulting in a decreasing trend of adsorption amount and removal rate.

$$F^- + H^+ \leftrightharpoons HF \quad (4)$$

$$HF + H^+ \leftrightharpoons HF^{2-} \quad (5)$$

Adsorption isotherms

In order to exhibit the mechanism of interaction between fluorine and the ACGC-Fe, we utilized the Langmuir and Freundlich models of adsorption isotherm to analyze and fit the experimental data obtained. The fitting curves for the adsorption isotherm can be observed in Fig. 6(b) and (c). The linear

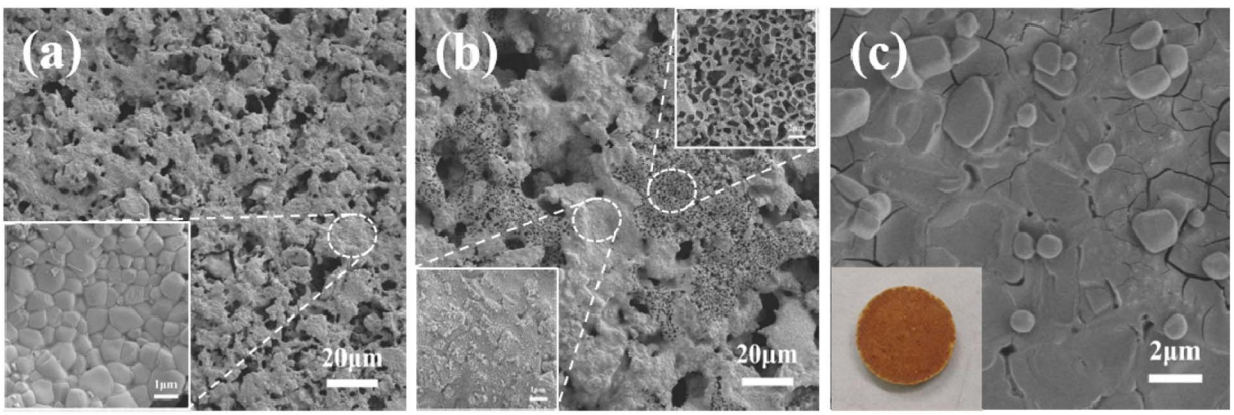

Fig. 4 SEM images. (a) CGC, (b) ACGC, (c) one side of ACGC-Fe.

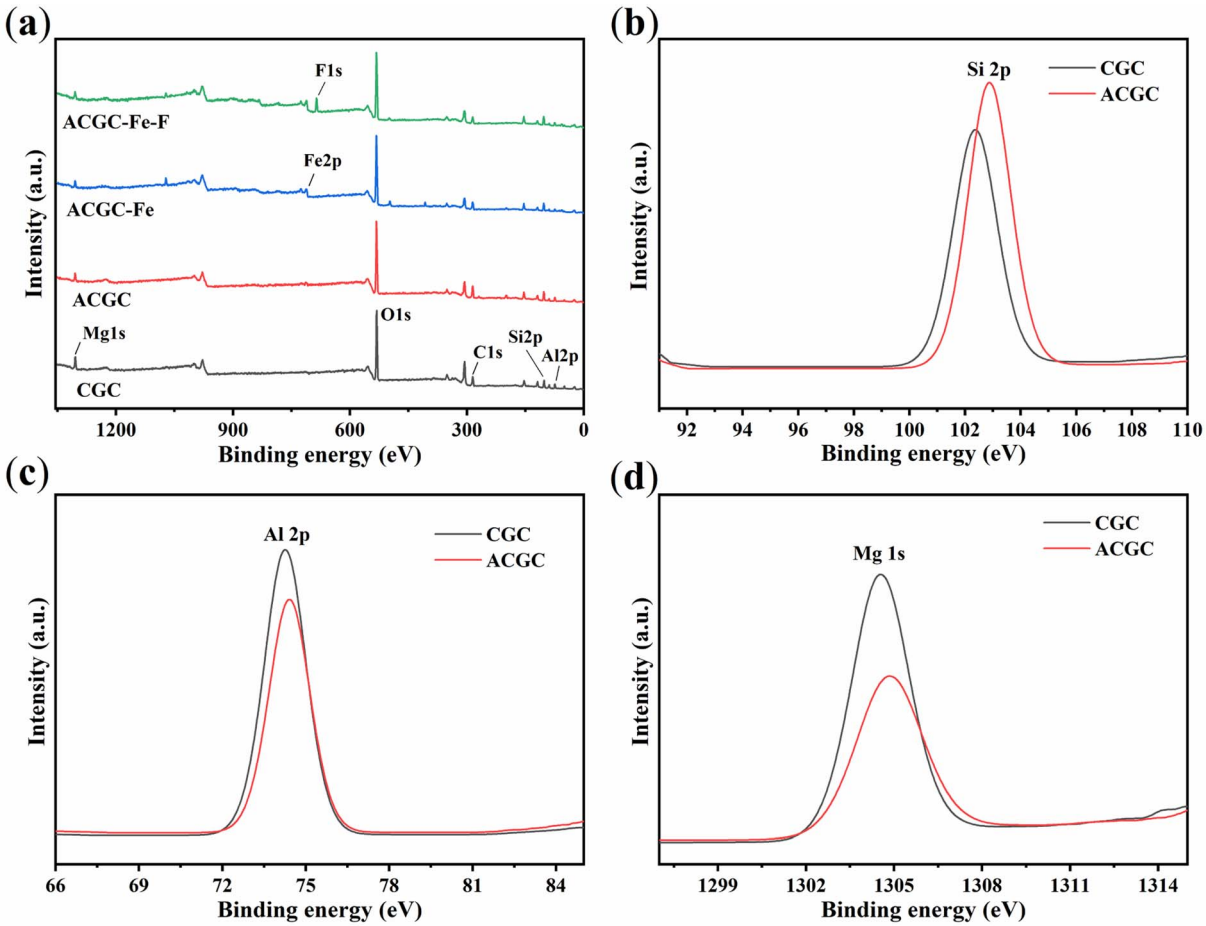

Fig. 5 (a) Full X-ray photoelectron spectroscopy (XPS) of CGC, ACGC, ACGC-Fe, and ACGC-Fe-F. High-resolution XPS spectra of (b) Si 2p, (c) Al 2p, (d) Mg 1s in CGC and ACGC.

equations for the Langmuir and Freundlich models of adsorption isothermal are shown in eqn (6)[40] and (7),[41] respectively.

$$\frac{C_e}{q_e} = \frac{C_e}{q_{max}} + \frac{1}{q_{max} \times k_L} \quad (6)$$

$$\ln q_e = \ln k_F + \frac{1}{n} \times \ln C_e \quad (7)$$

where C_e (mg L^{-1}) represents the concentration of the solution at the adsorption equilibrium stage, q_e (mg g^{-1}) denotes the amount of adsorbed fluorine at adsorption equilibrium, q_{max} refers to the maximum adsorption capacity, and k_L (L mg^{-1}) and k_F (mg g^{-1}) (L $mg^{-1})^{1/n}$, n represent the adsorption equilibrium constants of the linear equations corresponding to the isothermal models of Langmuir and Freundlich adsorption, respectively.

Table 2 presents the fitted parameters of the adsorption isothermal model for fluorine adsorption using ACGC-Fe. It is evident that the Freundlich model provides a slightly better fit, suggesting that ACGC-Fe adsorption of fluorine is based on both monolayer (chemisorption) and multilayer adsorptions (physisorption).[42] The value of the constant 'n' in the Freundlich model is in the range of 0 to 10,[43] indicating that ACGC-Fe adsorbs fluorine well and easily onto the sample. However, the Langmuir model can also fit the experimental data, yielding fit R^2 values greater than 0.96. This implies that the adsorption of fluorine on ACGC-Fe is influenced by various processes. Therefore, the process of fluorine adsorption on ACGC-Fe is governed by chemisorption and physisorption. We achieved a close resemblance between the actual experimental data and the calculated 'q_{max}' through the application of the Langmuir model.

Adsorption kinetics

To delve deeper into the interaction mechanism between ACGC-Fe and fluorine, we conducted simulations on the adsorption kinetics of the experimental data using three different models: pseudo-first-order, pseudo-second-order, and intra-particle diffusion. The results of these simulations are presented in Fig. 6(d), (e), and (f) respectively, and are based on the corresponding linear equations shown in eqn (8),[44] (9)[45] and (10)[46] respectively.

$$\log(q_e - q_t) = \log q_e - \left(\frac{k_1}{2.303}\right) \times t \quad (8)$$

$$\frac{t}{q_t} = \frac{1}{k_2 \times q_e^2} + \frac{t}{q_e} \quad (9)$$

$$q_t = k_{id} \times t^{\frac{1}{2}} + C_i \quad (10)$$

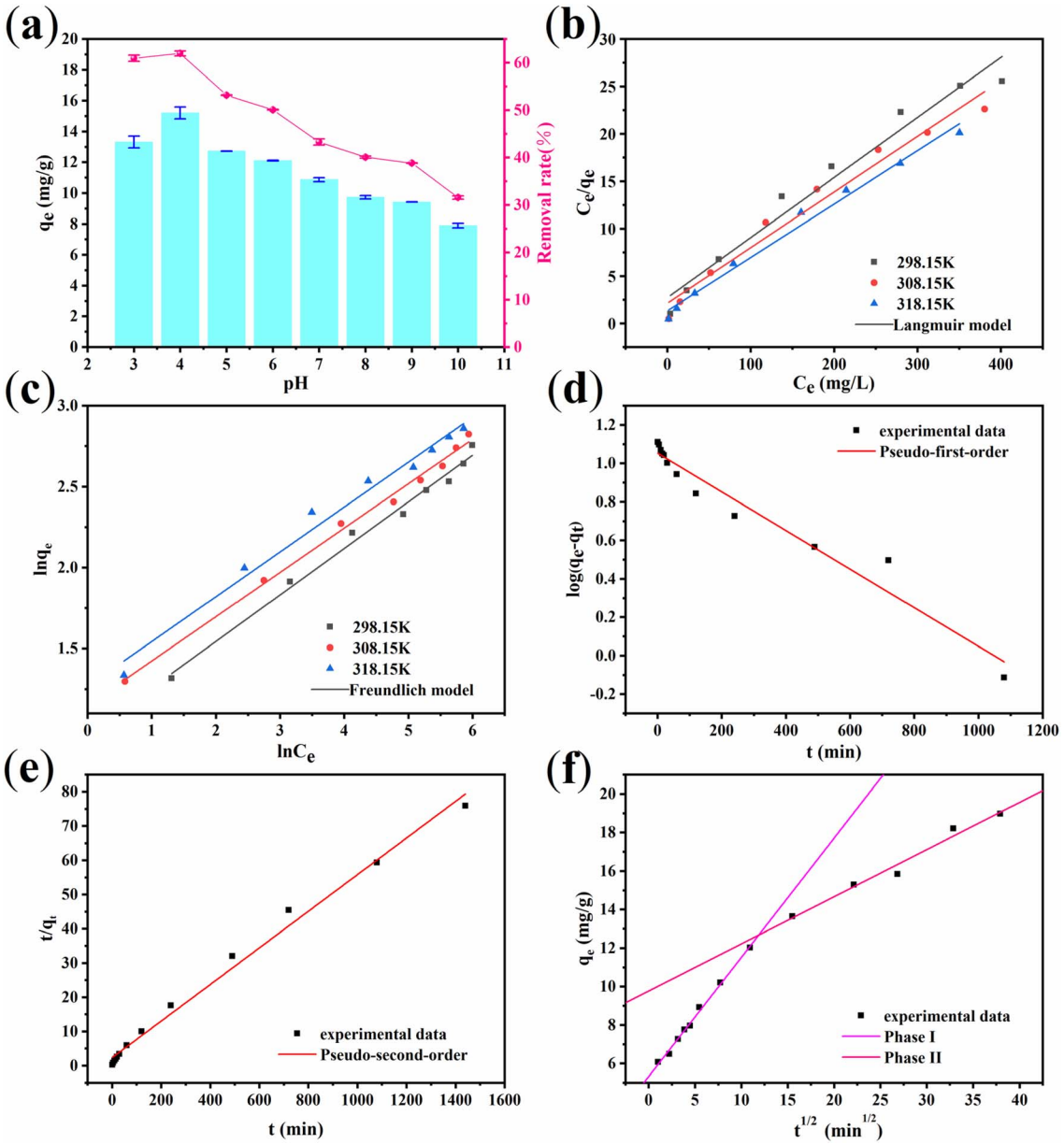

Fig. 6 (a) The effect of pH on the fluoride removal by ACGC-Fe (adsorption time = 12 h, initial fluoride concentration = 683 mg L^{-1}, temperature = 25 °C). Adsorption isotherm of fluoride removal by ACGC-Fe (pH = 4.0, adsorption time = 12 h). (b) Langmuir model. (c) Freundlich model. Adsorption kinetic model of fluoride removal by ACGC-Fe (pH = 4.0, temperature = 25 °C). (d) Pseudo-first-order. (e) Pseudo-second-order. (f) Intra-particle diffusion model.

Table 2 Langmuir model and Freundlich model parameters for fluoride adsorption on the ACGC-Fe

	Langmuir model			Freundlich model		
Temperature (K)	q_{max} (mg g^{-1})	k_L (L mg^{-1})	R^2	n	k_F (L g^{-1})	R^2
298.15 K	15.78	0.023	0.970	3.484	2.634	0.989
308.15 K	17.04	0.028	0.972	3.650	3.154	0.995
318.15 K	17.75	0.043	0.988	3.610	3.546	0.984

where q_e (mg g^{-1}) represents the amount of adsorbed fluorine at the adsorption equilibrium stage, q_t (mg g^{-1}) refers to the amount of adsorbed fluorine at a specific time, t (min) is the time, k_1 (min^{-1}), k_2 (g mg^{-1} min^{-1}) are the pseudo-first-order and pseudo-second-order adsorption rate constants respectively. Additionally, k_{id} (mg g^{-1} $min^{-1/2}$) denotes the intra-particle diffusion constant, and C_i represents the intercept of stage i.

Table 3 Adsorption kinetic parameters for fluoride adsorption on the ACGC-Fe

Temperature (K)		298.15 K
$q_{e,exp}$ (mg g^{-1})		18.97
Pseudo-first-order	k_1 (min^{-1})	0.0023
	$q_{e,cal}$ (mg g^{-1})	2.87
	R^2	0.958
Pseudo-second-order	k_2 (g mg^{-1} min^{-1})	0.0006
	$q_{e,cal}$ (mg g^{-1})	18.69
	R^2	0.991
Intra-particle diffusion model	k_{1d} (mg g^{-1} min$^{-1/2}$)	0.619
	k_{2d} (mg g^{-1} min$^{-1/2}$)	0.245

Table 3 exhibits the presented fitting parameters for the three distinct models. It becomes apparent that the pseudo-second-order model is outperformed by the pseudo-first-order model in describing the experimental data. Additionally, the calculated experimental adsorption capacity is similar to the actual adsorption capacity. As per the pseudo-second-order model, the adsorption process showcases the influence of various factors and is based on chemisorption,[47] indicating the involvement of chemical reactions[48] in the adsorption of fluorine by ACGC-Fe. In Fig. 6(f), the corresponding intra-particle diffusion model fit reveals two distinct adsorption regions.[49] The first region, characterized by a steeper slope, represents the fast adsorption rate or outer surface adsorption. The slower adsorption phase corresponds to the second region. The origin is not intersected by the two straight lines, implying that intraparticle diffusion is the factor controlling the rate, although it is not the sole factor.[47] At first, surface adsorption governs the process of adsorption because of the considerable concentration gradient between the adsorbent and the adsorbent. As the adsorption sites on the surface become saturated, fluorine gradually enters the ACGC-Fe pores and undergoes adsorption, which slows down due to intra-particle diffusion until adsorption equilibrium is reached. Therefore, the adsorption of fluorine by ACGC-Fe is regulated by surface diffusion and intra-particle diffusion.

Adsorption thermodynamics

In order to examine the thermodynamic behavior of the adsorption process, an experimental investigation of fluorine adsorption by ACGC-Fe was conducted in the temperature range of 298.15 K to 318.15 K. In order to analyze this, three essential thermodynamic parameters are considered: Gibbs free energy (ΔG), enthalpy change (ΔH), and entropy change (ΔS). These crucial parameters can be determined through the utilization of eqn (11),[50] (12)[51] and (13).[52] Fig. 7(a) illustrates a linear plot of ln k_c *versus* $1/T$. The *y*-intercept and slope of this plot correspond to the values of ΔS and ΔH, respectively.

$$\ln k_c = \ln \frac{q_e}{c_e} = \frac{\Delta S}{R} - \frac{\Delta H}{R \times T} \quad (11)$$

$$\Delta G = -RT \ln k_c \quad (12)$$

$$\Delta S = \frac{\Delta H - \Delta G}{T} \quad (13)$$

where k_c (L g^{-1}) denotes the distribution coefficient, q_e (mg g^{-1}) represents the amount of adsorbed fluorine at adsorption equilibrium, c_e (mg L^{-1}) indicates the concentration of the solution at the adsorption equilibrium stage, and $R = 8.314$ J mol^{-1} K^{-1}, T (K) represents the temperature.

The thermodynamic parameters for each temperature are shown in Table 4. The adsorption process of fluorine by ACGC-Fe is suggested to be endothermic, as indicated by the positive values of both ΔH and ΔS, and higher temperature promote this

Table 4 Thermodynamic parameters for fluoride adsorption on the ACGC-Fe

Temperature (K)	ΔH (kJ mol^{-1})	ΔS (kJ K^{-1}·mol^{-1})	ΔG (kJ mol^{-1})
298.15	2.144	0.013	−1.732
308.15			−1.862
318.15			−1.992

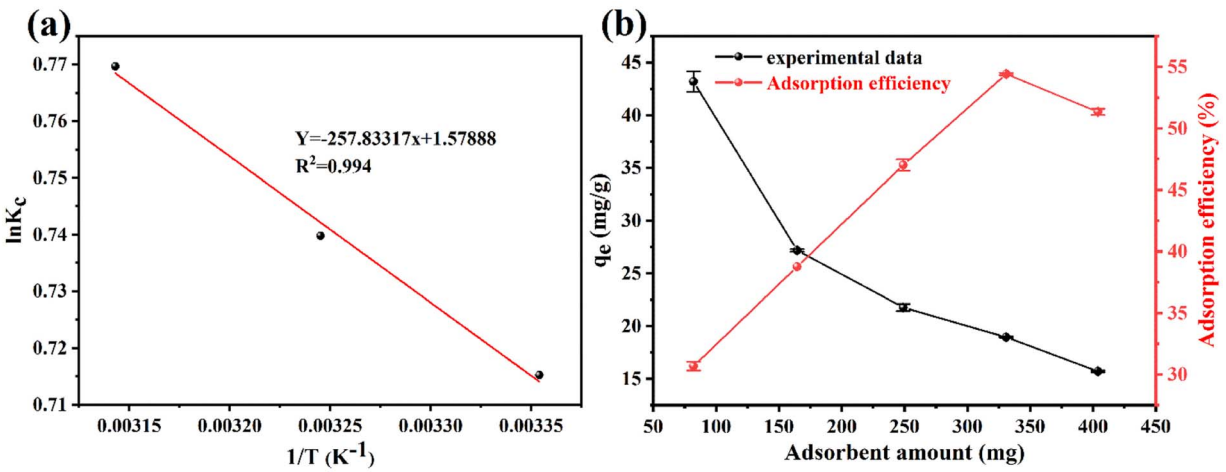

Fig. 7 (a) Linear plot of ln k_c *vs.* $1/T$ for the fluoride removal by ACGC-Fe. (b) The effect of ACGC-Fe dose on fluoride removal (adsorption time = 12 h, temperature = 25 °C, initial fluoride concentration = 769 mg L^{-1}).

adsorption. Additionally, the negative value of ΔG demonstrates the feasibility and spontaneous nature of the adsorption process. The decreasing trend of ΔG with increasing temperature also suggests that higher temperatures enhance the adsorption process.[53]

Effect of adsorbent amount

Adsorbent dosage is a crucial parameter in adsorption experiments. It is important to use an appropriate amount of adsorbent to achieve optimal adsorption without wastage. In Fig. 7(b), the influence of the adsorbent amount on the fluorine adsorption by ACGC-Fe adsorption is illustrated. As depicted in the figure, there is a gradual decline in the amount of adsorption with the increasing adsorbent quantity. The rationale behind this observation can be attributed to the breakdown of the adsorbent amount into the mass of CGC and the mass of polyhydroxy iron. Notably, the mass of polyhydroxy iron, which plays the main adsorption role, remained relatively stable during the increase in adsorbent amount. The rate of removal exhibited a pattern of ascending and then descending. Consequently, we determined the optimal adsorbent dosage to be approximately 331 mg, corresponding to the highest removal rate.

Adsorption mechanism

The crucial role played by the adsorption mechanism is significant in the examination of material characteristics. To explore the adsorption of fluoride by ACGC-Fe, the chemical composition and chemical state of the samples were evaluated pre and post-adsorption utilizing XPS analysis. Fig. 5(a) depicts the XPS profiles of ACGC-Fe and ACGC-Fe-F. Compared to ACGC-Fe, ACGC-Fe-F reveals new peaks. This peak is attributed to the adsorption of fluorine, which is attributed to F 1s. The higher binding energy of F 1s compared to sodium fluoride (684.50 eV),[54] confirms that fluorine interacts with the metal[55] and validates the successful adsorption of fluorine into the sample. Further, a split peak was fitted to the F 1s peak as shown in Fig. 8(a), where one of the split peaks has a binding energy of 684.57 eV, corresponding to Fe–F.[55] This indicates the adsorption of fluorine by polyhydroxy iron. The comparative spectra of Al 2p and Mg 1s in Fig. 8(b) and (c), respectively, indicate that their binding energies increased after the adsorption of fluorine. This suggests a strong interaction between Al^{3+}, Mg^{2+}, and fluorine.[56] Likewise, Fig. 8(d) presents a comparison of the O 1s spectra before and after the adsorption process, revealing an increase in the binding energy of the

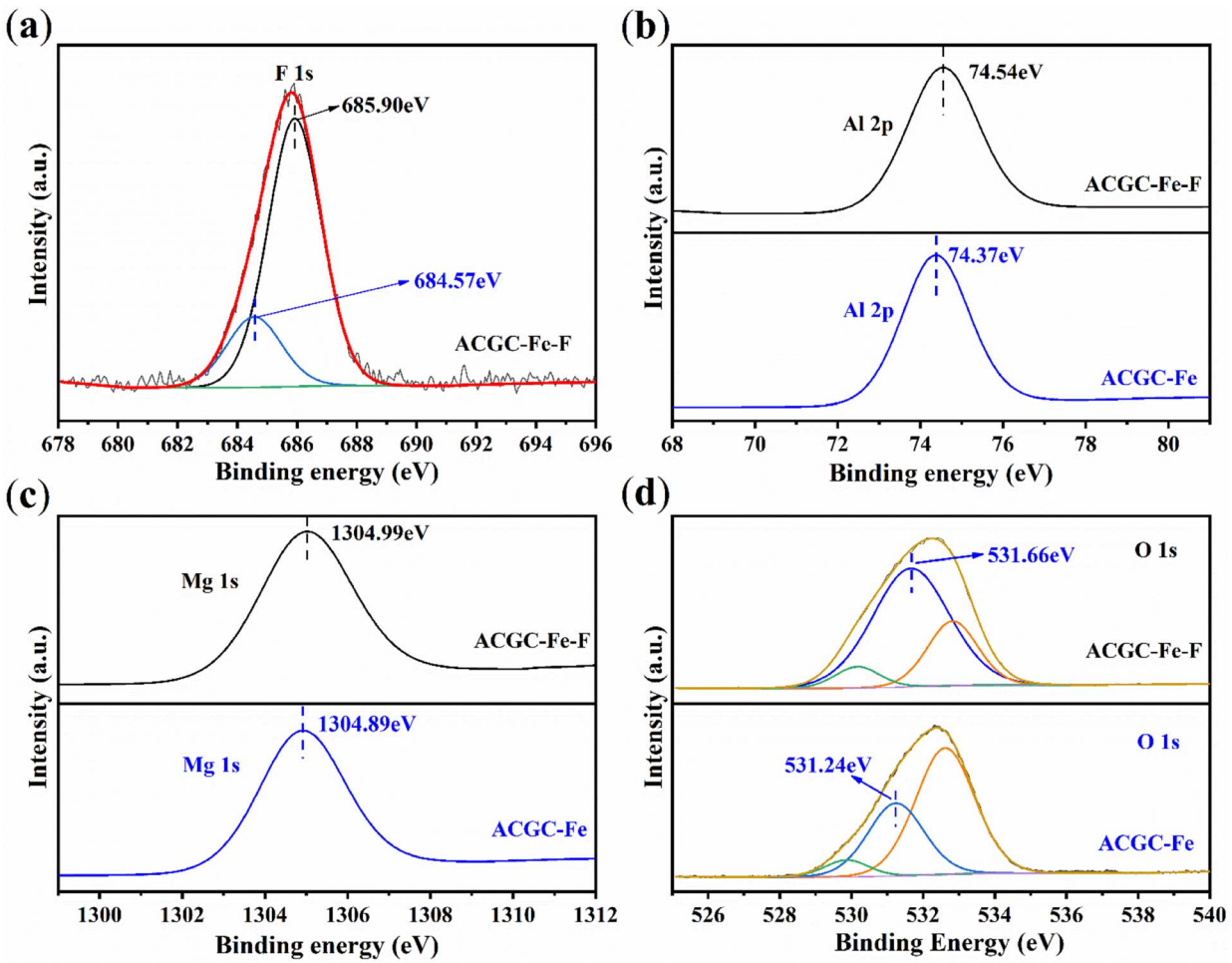

Fig. 8 High-resolution XPS spectra. (a) F 1s of ACGC-Fe-F. (b) Al 2p, (c) Mg 1s, (d) O 1s of ACGC-Fe and ACGC-Fe-F.

defective oxygen (O_{def}/–OH) located around 531 eV.[57] This increase is attributed to the hydroxyl groups on the surface of ACGC-Fe that combine with fluorine to form hydrogen bonds during the reaction, resulting in the trapping of fluorine. Thus, the adsorption of fluorine by ACGC-Fe occurs through two mechanisms: hydrogen bonding with hydroxyl groups and bonding with metal ions.

Conclusion

Portable hydroxyl-functionalized coal gangue-based cordierite porous ceramics sheets were fabricated using powder compression molding and mild chemical modification. These ceramics can effectively remove fluoride in simulated wastewater, achieving a maximum adsorption capacity of 18.69 mg g^{-1}. The Langmuir (Freundlich) adsorption isotherm model and pseudo-second-order kinetic model were found to be the most appropriate for describing the adsorption mechanism of ACGC-Fe for fluoride. This confirms that at pH = 4, the adsorption mechanism consists of cumulative interactions dominated by the chemisorption of hydrogen bonds (with hydroxyl group) and ionic bonds (with metal), as well as physical adsorption based on cordierite porous ceramic pores.

Author contributions

Deyin Wang: conceptualization, formal analysis, investigation, visualization, writing – original draft. Liming Guo: investigation, validation, writing – review& editing. Zhennan Qiao: investigation, writing – review& editing. Hongwei Liu: conceptualization, supervision. Yanlan Zhang: supervision. Yongzhen Wang: funding acquisition, writing – review & editing.

Conflicts of interest

The authors declare that they have no known competing financial interests or personal relationships that could have appeared to influence the work reported in this paper.

Acknowledgements

This work was supported by National Natural Science Foundation of China (Grant number: 52371231), Central Government Guides Local Science and Technology Development Special Fund Project (Grant number: YDZJSX2022B003).

References

1 S. You, S. Cao, C. Mo, Y. Zhang and J. Lu, *Chem. Eng. J.*, 2023, **453**, 139733.
2 Y. Qiu, L.-F. Ren, J. Shao, L. Xia and Y. Zhao, *J. Cleaner Prod.*, 2022, **349**, 131225.
3 F. Ahmadijokani, H. Molavi, M. Rezakazemi, T. M. Aminabhavi and M. Arjmand, *Coord. Chem. Rev.*, 2021, **445**, 214037.
4 C. F. Z. Lacson, M.-C. Lu and Y.-H. Huang, *J. Cleaner Prod.*, 2021, **280**, 124236.
5 M. Barathi, A. S. K. Kumar and N. Rajesh, *Coord. Chem. Rev.*, 2019, **387**, 121–128.
6 X. Wang, J. Wang, W. Li and J. Zhang, *Sep. Purif. Technol.*, 2023, **310**, 122933.
7 W. J. Xu, Q. L. He, S. J. Zhang and W. S. Zhang, *Polym. Bull.*, 2018, **75**, 1171–1184.
8 A. Naghizadeh and K. Gholami, *J. Water Health*, 2017, **15**, 555–565.
9 A. S. Jadhav and M. V. Jadhav, *Korean J. Chem. Eng.*, 2021, **38**, 2082–2090.
10 Z. Jin, Y. Jia, K.-S. Zhang, L.-T. Kong, B. Sun, W. Shen, F.-L. Meng and J.-H. Liu, *J. Alloys Compd.*, 2016, **675**, 292–300.
11 J.-Y. Lin, Y.-L. Chen, X.-Y. Hong, C. Huang and C. P. Huang, *J. Colloid Interface Sci.*, 2020, **561**, 275–286.
12 J. Xiao, F. Li, Q. Zhong, H. Bao, B. Wang, J. Huang and Y. Zhang, *Hydrometallurgy*, 2015, **155**, 118–124.
13 Z. Sun, Y. Hu, K. Zeng, M. Li, S. Zhao and J. Zhang, *Small*, 2023, **19**, 2208145.
14 W. Guo, B. Chen, G. Li, M. Liu, X. Liu, Q. Chen, X. Zhang, S. Li, S. Chen, W. Feng, R. Zhang, M. Chen and T. Shi, *Environ. Sci. Technol.*, 2021, **55**, 5763–5771.
15 H. Gao, Y. Huang, W. Li, J. Li, S. Ouyang, T. Song, F. Lv, W. Zhai and K. Ma, *Environ. Sci. Pollut. Res.*, 2021, **28**, 65363–65373.
16 Z. Yang, Y. Zhang, L. Liu, X. Wang and Z. Zhang, *Waste Manage.*, 2016, **50**, 213–221.
17 Y. Zhao, J. Qiu, Z. Ma and X. Sun, *J. Cleaner Prod.*, 2021, **285**, 124834.
18 J. Zhao, Q. Liu, B. Long, Z. Cheng, H. Wang and D. Wang, *Fuel*, 2023, **345**, 128185.
19 Y. Jin, L. Li, Z. Liu, S. Zhu and D. Wang, *Adv. Powder Technol.*, 2021, **32**, 791–801.
20 J. Gao, Q. Lin, T. Yang, Y. c. Bao and J. Liu, *Chemosphere*, 2023, **341**, 139741.
21 X. Lao, Z. Tu, X. Xu, W. Jiang and J. Liang, *J. Cleaner Prod.*, 2023, **383**, 135383.
22 T. Zhang, H. Yang, H. Zhang, P. Zhang and R. Bei, *J. Anal. Appl. Pyrolysis*, 2022, **163**, 105504.
23 Y. Zhang, Z. Wei, M. Li, X. Wu and W. Wang, *ACS Omega*, 2020, **5**, 15691–15701.
24 S. Yang, Q. Cheng, L. Hu, Y. Gu, Y. Wang and Z. Liu, *ACS Omega*, 2023, **8**, 11457–11466.
25 A. N. Shigapov, G. W. Graham, R. W. McCabe, M. Paputa Peck and H. Kiel Plummer, *Appl. Catal., A*, 1999, **182**, 137–146.
26 T. Muschin, H. Zulchin and M. Jia, *ChemistrySelect*, 2021, **6**, 3075–3083.
27 T. Ai, X. Jiang, Q. Liu, L. Lv and S. Dai, *RSC Adv.*, 2020, **10**, 20427–20437.
28 J. Lu, H. Wei, R. Peng, B. Liu and X. He, *J. Environ. Chem. Eng.*, 2024, **12**, 111684.
29 Z. Yuanyuan, G. Yanxia, C. Fangqin, Y. Kezhou and C. Yan, *Thermochim. Acta*, 2015, **614**, 137–148.
30 J. Ren, C. J. Xie, X. Guo, Z. F. Qin, J. Y. Lin and Z. Li, *Energy Fuels*, 2014, **28**, 3688–3695.

31 Q. Wang, H. Wang, B. Sun, J. Bai and X. Guan, *Fuel*, 2009, **88**, 1520–1529.
32 X. Ma, C. Ding, H. Yang and X. Zhu, *Materials*, 2023, **16**, 3896.
33 H. Kim, H. Jeong and S.-H. Byeon, *ACS Appl. Mater. Interfaces*, 2016, **8**, 15497–15505.
34 M. T. Aytekin and H. L. Hoşgün, *Chem. Pap.*, 2020, **74**, 4547–4557.
35 E. A. Ofudje, A. E. Adedapo, O. B. Oladeji, E. F. Sodiya, F. H. Ibadin and D. Zhang, *J. Environ. Chem. Eng.*, 2021, **9**, 105931.
36 H. Liu, Y. Wang, L. Lv, X. Liu, Z. Wang and J. Liu, *Energy*, 2023, **269**, 126707.
37 C. Yang and Y. Xia, *ACS Appl. Nano Mater.*, 2022, **5**, 5268–5277.
38 M. M. Damtie, Y. C. Woo, B. Kim, R. H. Hailemariam, K.-D. Park, H. K. Shon, C. Park and J.-S. Choi, *J. Environ. Manage.*, 2019, **251**, 109524.
39 J. Deng, Z. Ma, Q. Qin, W. Liu and B. Wang, *J. Cleaner Prod.*, 2022, **371**, 133613.
40 I. Takanashi, T. Kameda, S. Kumagai, Y. Saito, Y. Nomura, D. Kawamura and T. Yoshioka, *J. Alloys Compd.*, 2023, **960**, 170865.
41 W. Huang, Y. Xu, N. Chen, G. Cheng and H. Ke, *J. Environ. Chem. Eng.*, 2023, **11**, 111441.
42 V. Srivastava, M. Shekhar, D. Gusain, F. Gode and Y. C. Sharma, *Arabian J. Chem.*, 2017, **10**, S3073–S3083.
43 M. K. Habibi, S. M. Rafiaei, A. Alhaji and M. Zare, *J. Alloys Compd.*, 2022, **890**, 161901.
44 S. Duengsuwan, S. Sangon, P. Noppawan, Y. Ngernyen, D. MacQuarrie, J. L. Scott, N. Supanchaiyamat and A. J. Hunt, *J. Environ. Chem. Eng.*, 2023, **11**, 111361.
45 P. T. Tho, H. T. Van, L. H. Nguyen, T. K. Hoang, T. N. Ha Tran, T. T. Nguyen, T. B. Hanh Nguyen, V. Q. Nguyen, H. Le Sy, V. N. Thai, Q. B. Tran, S. M. Sadeghzadeh, R. Asadpour and P. Q. Thang, *RSC Adv.*, 2021, **11**, 18881–18897.
46 Z. Zeng, Q. Li, J. Yan, L. Huang, S. R. B. Arulmani, H. Zhang, S. Xie and W. Sio, *Chemosphere*, 2023, **340**, 139808.
47 Z. Wang, J. Su, X. Hu, A. Ali and Z. Wu, *J. Hazard. Mater.*, 2021, **406**, 124748.
48 C. H. Bolster, *Chemosphere*, 2023, **345**, 140523.
49 S. Jiang, T. Yu, R. Xia, X. Wang and M. Gao, *Mater. Chem. Phys.*, 2019, **232**, 374–381.
50 Y. Wang, K. Li, L. Ma, D. Fang, M. Lu, X. Ye, H. Liu, H. Zhang, X. Tan and Z. Wu, *Hydrometallurgy*, 2023, **216**, 106011.
51 H. Sid Kalal, H. Rashedi, Z. Shiri-Yekta and M. Taghiof, *Microporous Mesoporous Mater.*, 2024, **366**, 112944.
52 G. Bazarin, A. N. Módenes, F. R. Espinoza-Quiñones, C. E. Borba, D. E. G. Trigueros and I. C. Dall'Oglio, *J. Environ. Chem. Eng.*, 2024, **12**, 111761.
53 M. Li, X. Chen, J. He, S. Liu, Y. Tang and X. Wen, *J. Alloys Compd.*, 2023, 173107.
54 J. Wei, X. Wang, X. Lv, G. Lv, J. Wang and J. Zhang, *J. Chin. Chem. Soc.*, 2022, **69**, 1669–1679.
55 X. Wu, Y. Zhang, X. Dou, B. Zhao and M. Yang, *Chem. Eng. J.*, 2013, **223**, 364–370.
56 X. Wang, J. Wei, W. Peng, J. Dan, J. Wang and J. Zhang, *Appl. Surf. Sci.*, 2021, **552**, 149423.
57 J. Tian, K. Zhang, W. Wang, F. Wang, J. Dan, S. Yang, J. Zhang, B. Dai and F. Yu, *Green Energy Environ.*, 2019, **4**, 311–321.